



Numerical simulation of TEM images for In(Ga)As/GaAs quantum dots with various shapes

Anieza Maltsi¹ · Tore Niermann² · Timo Streckenbach¹ · Karsten Tabelow¹ · Thomas Koprucki¹

Received: 13 September 2019 / Accepted: 10 April 2020
© The Author(s) 2020, corrected publication 2021

Abstract

We present a mathematical model and a tool chain for the numerical simulation of TEM images of semiconductor quantum dots (QDs). This includes elasticity theory to obtain the strain profile coupled with the Darwin–Howie–Whelan equations, describing the propagation of the electron wave through the sample. We perform a simulation study on indium gallium arsenide QDs with different shapes and compare the resulting TEM images to experimental ones. This tool chain can be applied to generate a database of simulated TEM images, which is a key element of a novel concept for model-based geometry reconstruction of semiconductor QDs, involving machine learning techniques.

Keywords Semiconductors · Quantum dots · TEM images · Electron wave propagation · Strain

1 Introduction

The fabrication of semiconductor quantum dots (QDs) with specific electronic properties would highly benefit from the assessment of QD geometry, distribution, and strain profile in a feedback loop between epitaxial growth and analysis of their properties. To assist the

Funded by the Deutsche Forschungsgemeinschaft (DFG, German Research Foundation) under Germany's Excellence Strategy—MATH+: The Berlin Mathematics Research Center, EXC-2046/1—Project ID: 390685689 (A.M) and within CRC 787 “Semiconductor Nanophotonics” under Project A4 (T.N).

This article is part of the Topical Collection on Numerical Simulation of Optoelectronic Devices.

Guest edited by Angela Thränhardt, Karin Hinzer, Weida Hu, Stefan Schulz, Slawomir Sujecki and Yuhrenn Wu.

✉ Anieza Maltsi
anieza.maltsi@wias-berlin.de

¹ Weierstrass Institute (WIAS), Mohrenstr. 39, 10117 Berlin, Germany

² Institut für Optik und Atomare Physik, Technische Universität Berlin, Straße des 17. Juni 135, 10623 Berlin, Germany

optimization of QDs transmission electron microscopy (TEM) can be used. However, a direct 3D geometry reconstruction from TEM of bulk-like samples (thickness 100–200 nm) by solving the tomography problem is not feasible due to its limited resolution (0.5–1 nm), the highly nonlinear behaviour of the dynamic electron scattering and strong stochastic influences in the images.

Recently, we introduced a novel concept for 3D *model-based geometry reconstruction* (MBGR) of QDs from TEM imaging (Koprucki et al. 2018; Maltzi et al. 2018). The approach is based on (a) an appropriate model for the QD configuration in real space including a categorization of QD shapes (e.g. pyramidal or lens-shaped) and continuous parameters (e.g. size, height), (b) a database of simulated TEM images covering a large number of possible QD configurations and image acquisition parameters (e.g. bright field/dark field, sample tilt), as well as (c) a statistical procedure for the estimation of QD properties and classification of QD types based on acquired TEM image data.

Here, we present as a first step towards MBGR: A mathematical model and a tool chain for the numerical simulation of TEM images for semiconductor QDs. We perform a simulation study on lens-shaped and pyramidal indium gallium arsenide QDs embedded in a gallium arsenide matrix and compare the resulting TEM simulations to experimental derived images. It is known that TEM images are very sensitive to strain fields around QDs and these fields are mostly responsible for the observed contrast. In order to link the contrasts in TEM images with shapes and concentration of these QDs it is crucial to combine strain calculations with TEM image simulations. Previous examples of investigations with combined finite element and image calculations include the explanation of surface relaxation contrasts along quantum wells by Jacob et al. (1998) and explanation of the typical coffee-bean contrast around QDs by Benabbas et al. (1996). Previous observations of Liao et al. (1998) showed that, for single excitation conditions, it is hard to distinguish between effects of shape and crystal symmetries on the TEM images. By our systematic study of the influence of the shape on the image contrast, we could identify excitation conditions that allow to distinguish between lens-shaped and pyramidal QDs.

2 Imaging of quantum dots by transmission electron microscope

The principal ray path for conventional imaging of crystalline specimen within a TEM is sketched in Fig. 1. A parallel electron beam illuminates a specimen of typical thicknesses below few hundred nanometers.

The periodic structure of the specimen diffracts the beam in discrete directions, which fulfill the Laue condition for a certain reciprocal lattice point \mathbf{g} . Due to the finite extent of the specimen in the beam direction, the Laue condition must not be exactly fulfilled. Figure 1c, d illustrates two possible cases, in the latter only two beams are exactly on the Ewald sphere (two beam conditions).

The diffracted beams leaving the exit surface of the specimen are focussed again by the objective into a magnified image of the specimen. The objective aperture allows to restrict the set of transmitted beams forming this image. In general, the term *bright field* image is used, when the undiffracted beam is included in the aperture (e.g. Fig. 1a). Here we use the term *dark field* for images, where only one diffracted beam forms the image (Fig. 1b).

As further detailed in Sect. 3 the obtained images in two beam conditions are mostly sensitive to the displacement field components along the direction of the diffraction vector \mathbf{g} . Examples for TEM images of two QDs are shown in Fig. 2. These are dark field images

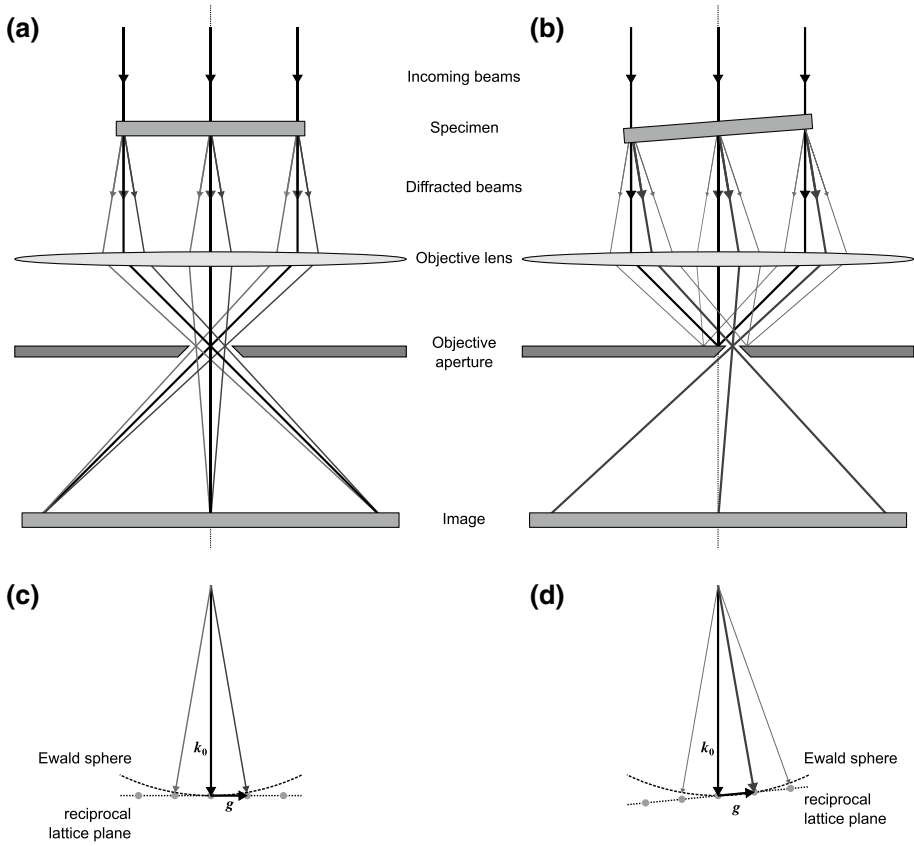
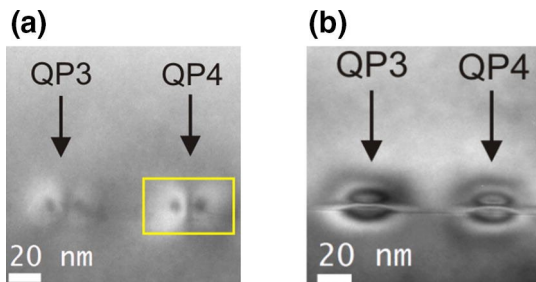


Fig. 1 Ray path within TEM: **a** ray path for imaging a specimen, with the objective aperture selecting all beams. **b** Ray path for a specimen in two beam conditions, where the objective aperture only selects the strongly excited beam. **c** Ewald sphere for case **a**, **d** Ewald sphere for case **b**

Fig. 2 TEM images of InAs QDs: **a** dark field of (040) beam, sensitive to [010]-component of strain, **b** dark field of (004) beam, sensitive to [001]-component of strain, adapted from Hartwig (2011), both showing a coffee-bean-like contrast. ©2018 IEEE. Reprinted, with permission, from Koprucki et al. (2018)



of the excited beam obtained for two beam conditions, in two perpendicular directions. Both images are showing a coffee-bean-like contrast along the direction of the respective diffraction vector.

This sensitivity for certain components of the displacement field is also used for instance in dislocation imaging. Depending on the dislocation type the displacement field has no

component in certain directions. These directions can be found by looking for diminishing contrast under two-beam conditions for different diffraction vectors \mathbf{g} . Typically the contrast vanishes for directions \mathbf{g} perpendicular to the Burger’s vector of the dislocation, i.e. $\mathbf{g} \cdot \mathbf{b} = 0$ (De Graef 2003).

3 Modeling of TEM imaging of semiconductor nanostructures

The dynamical electron scattering in crystalline solids, e.g. semiconductor nanostructures, is influenced by spatial variations in the material composition and by local deformations of the lattice due to elastic strain. In order to model the TEM images we need to use elasticity theory to obtain the strain profile and couple this with the equations describing the electron propagation through the sample.

The indium gallium arsenide QDs under consideration and the surrounding GaAs matrix have different lattice constants. This induces mechanical stresses in the nanostructure. The strain tensor is defined as $\boldsymbol{\varepsilon}(\mathbf{u}) = \frac{1}{2}(\nabla\mathbf{u} + (\nabla\mathbf{u})^T)$, where the displacement $\mathbf{u} : \Omega \rightarrow \mathbb{R}^3$ and the stress $\boldsymbol{\sigma}$ is linked to the strain by Hook’s law $\boldsymbol{\sigma} = \mathbf{C} : \boldsymbol{\varepsilon}$. Here, \mathbf{C} is the elastic stiffness tensor.

We model the elastic relaxation of the misfit-induced strain following the concept of Eshelby’s inclusion (Eshelby 1957). The approach was developed for the description of the elastic relaxation within and around *inclusions* of a solid surrounded by a *matrix*. The GaAs matrix provides a *global reference* for measuring displacements and strains. For simplicity we assume that both matrix and inclusion (QD) exhibit cubic symmetry. If we remove the inclusion from the matrix, it is stress-free, if the strain $\boldsymbol{\varepsilon}$ of the reference system equals the eigenstrain $\boldsymbol{\varepsilon}^*$. Assuming a stress-strain relation according to Hooke’s law, we can mimic the stress-free condition for $\boldsymbol{\varepsilon} = \boldsymbol{\varepsilon}^*$ in the reference system of the matrix by incorporating the eigenstress in the momentum balance:

$$\nabla \cdot (\boldsymbol{\sigma} - \boldsymbol{\sigma}^*) = 0. \tag{1}$$

The boundary condition on the Neumann part of the boundary (stress-free relaxation) has to be modified accordingly

$$(\boldsymbol{\sigma} - \boldsymbol{\sigma}^*) \cdot \mathbf{n} = 0. \tag{2}$$

The dynamical electron scattering is described by the Schrödinger equation,

$$\Delta\Psi + 4\pi^2\mathbf{k}_0^2\Psi = -4\pi^2U(\mathbf{r})\Psi, \tag{3}$$

where $\mathbf{k}_0 \in \mathbb{R}^3$ describes the incoming electron beam and $U(\mathbf{r})$ the reduced electrostatic lattice potential. We assume a propagation of the beam in x -direction. Writing the wave function as a superposition of plane waves, for the directions given by the Laue condition:

$$\Psi(\mathbf{r}) = \sum_{\mathbf{g}} \psi_{\mathbf{g}}(x,y,z)e^{2\pi i(\mathbf{k}_0+\mathbf{g})\cdot\mathbf{r}}, \quad \mathbf{r} = (x,y,z). \tag{4}$$

we end up with the Darwin–Howie–Whelan equations (De Graef 2003)

$$\frac{d\psi_{\mathbf{g}}}{dx} = i\pi \left[2s_{\mathbf{g}}\psi_{\mathbf{g}} + \frac{1}{\mathbf{n} \cdot (\mathbf{k}_0 + \mathbf{g})} \sum_{\mathbf{g}'} U_{\mathbf{g}-\mathbf{g}'}\psi_{\mathbf{g}'} \right], \quad s_{\mathbf{g}} = -\frac{\mathbf{g} \cdot (2\mathbf{k}_0 + \mathbf{g})}{2\mathbf{n} \cdot (\mathbf{k}_0 + \mathbf{g})}. \tag{5}$$

The amplitudes $\psi_{\mathbf{g}}$ depend only parametrically on the (y, z) -coordinates, which define a 2D pixel array constituting the TEM image. The Fourier coefficients $U_{\mathbf{g}}$ of the reduced electrostatic potential $U(\mathbf{r})$ of the crystal introduce a coupling between the beams and the excitation error $s_{\mathbf{g}}$ shows how well the Laue condition is satisfied. We consider only amplitudes $\psi_{\mathbf{g}}$ with a small excitation error $s_{\mathbf{g}}$. In our case the vector \mathbf{n} is the unit vector in x direction.

The influence of variations in the indium content $c(\mathbf{r})$ and of the lattice deformations given by the displacement field $\mathbf{u}(\mathbf{r})$ can be approximated by the modification of the Fourier coefficients according to

$$U_{\mathbf{g}} \rightarrow U'_{\mathbf{g}}(\mathbf{r}) = [c(\mathbf{r})U_{\mathbf{g}}^{\text{InAs}} + (1 - c(\mathbf{r}))U_{\mathbf{g}}^{\text{GaAs}}] \times \exp(-2\pi i \mathbf{u}(\mathbf{r}) \cdot \mathbf{g}). \tag{6}$$

The projection of the displacement on the individual reciprocal lattice vector \mathbf{g} enters the coupling as phase factor.

4 Numerical simulation of TEM images for different geometries

A simulated TEM image is generated by propagating the beams through the specimen for every pixel (y_i, z_j) , $i, j = 1, \dots, N$. This is done numerically by solving the Darwin–Howie–Whelan equations (5) using displacements \mathbf{u} obtained from the elasticity problem (1) for a given geometry.

The excitation errors $s_{\mathbf{g}}$ entering the Darwin–Howie–Whelan equations depend on the orientation of the crystallographic lattice with respect to the beam direction. The specimen can be oriented such that only a small number of beams \mathbf{g} with amplitudes $\psi_{\mathbf{g}}$ are excited. For two-beam conditions, the Ewald sphere only cuts two reciprocal lattice points. Thereby, most of the intensity is contained within the undiffracted ψ_0 and a single diffracted beam $\psi_{\mathbf{g}}$ while the other beams remain largely unexcited, see Fig. 1d.

In imaging conditions, where the objective aperture selects only a single beam, the image contrast is simply obtained by taking the square of the modulus of the beam’s amplitude at the exit plane $x = x_{\text{exit}}$

$$I_{\mathbf{g}}(y, z) = |\psi_{\mathbf{g}}(x_{\text{exit}}; y, z)|^2. \tag{7}$$

For example for excitation of (040)-two beam conditions, the bright field is given by $I_0(y, z)$ while the dark field image is given by $I_{\mathbf{g}}(y, z)$ with $\mathbf{g} = (040)$.

4.1 Tool chain for simulation of TEM images

The simulation tool chain starts with a parametric geometry description of the QD shape, e.g. using base length and height of the pyramidal QD. A representation of the geometry by a triangulation is created using the 3D mesh generator TetGen (Si 2015), see Fig. 5a. The generated mesh enters a FEM-based elasticity solver of WIAS-pdelib (Fuhrmann et al. 2019) which computes the strain profile and the displacement field \mathbf{u} in the QD and in the sample. Finally, the multi-beam solution is obtained by the Darwin–Howie–Whelan solver pyTEM (Niermann 2019) depending on excitation conditions and the sample orientation and results in the simulated TEM image. For the examples shown in the following we assumed an acceleration voltage of 300 kV. The y and z range of the simulated TEM images is -50 nm to 50 nm around the center of the quantum dot, sampled with 101 points. The beams used are chosen from (020) systematic row for the (040) reflection and (002)

systematic row for the (004) reflection. From these, the beams with the smallest excitation error were used (6 beams in our case).

4.2 Spherical QD

As a first example, we consider a spherical InAs QD with radius 10 nm embedded in a GaAs matrix. Figure 3b shows the dark field TEM image under (040)-two beam conditions, revealing a coffee-bean like contrast which looks similar to the experimental results shown in Fig. 2. For comparison Fig. 3a shows a simulated TEM image using in Eq. (6) the effect of the material contrast only, neglecting strain effects. Even the qualitative behavior differs strongly from the results of the fully-coupled simulation (Fig. 3b) and from the experimental observations (Fig. 2). This demonstrates that the TEM contrast is dominated by the strain profile around the QD, shown in Fig. 3c, and the nonlocal behavior of the mapping QD geometry (sphere) to TEM image (coffee-bean).

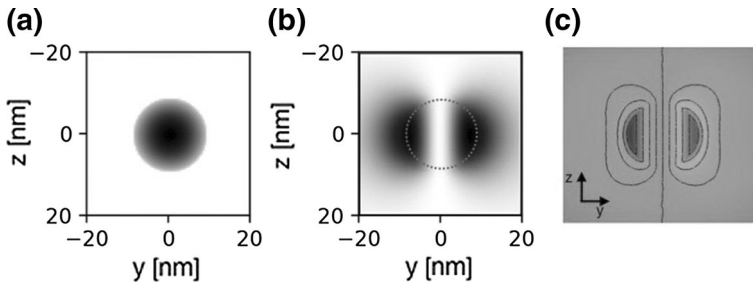


Fig. 3 Simulated TEM images: **a** dark field for material contrast only, **b** dark field also including influence of strain. The image contrast in **a** is strongly increased for better visualization. Due to the excitation under (040)-two-beam conditions, the image contrast is sensitive to the [010]-component of the displacement field, shown in **c** along a cross-section through the center of a spherical InAs QD as obtained by FEM. ©2018 IEEE. Reprinted, with permission, from Koprucki et al. (2018)

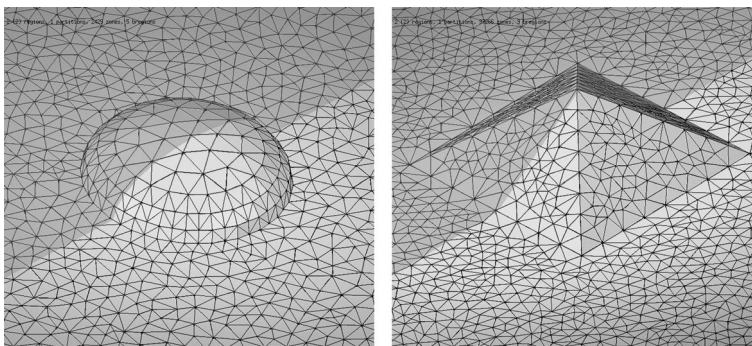


Fig. 4 3D view of the geometry of a lens-shaped and a pyramidal quantum dot. The shadow indicates the cutting plane for the cross sections shown in Fig. 5

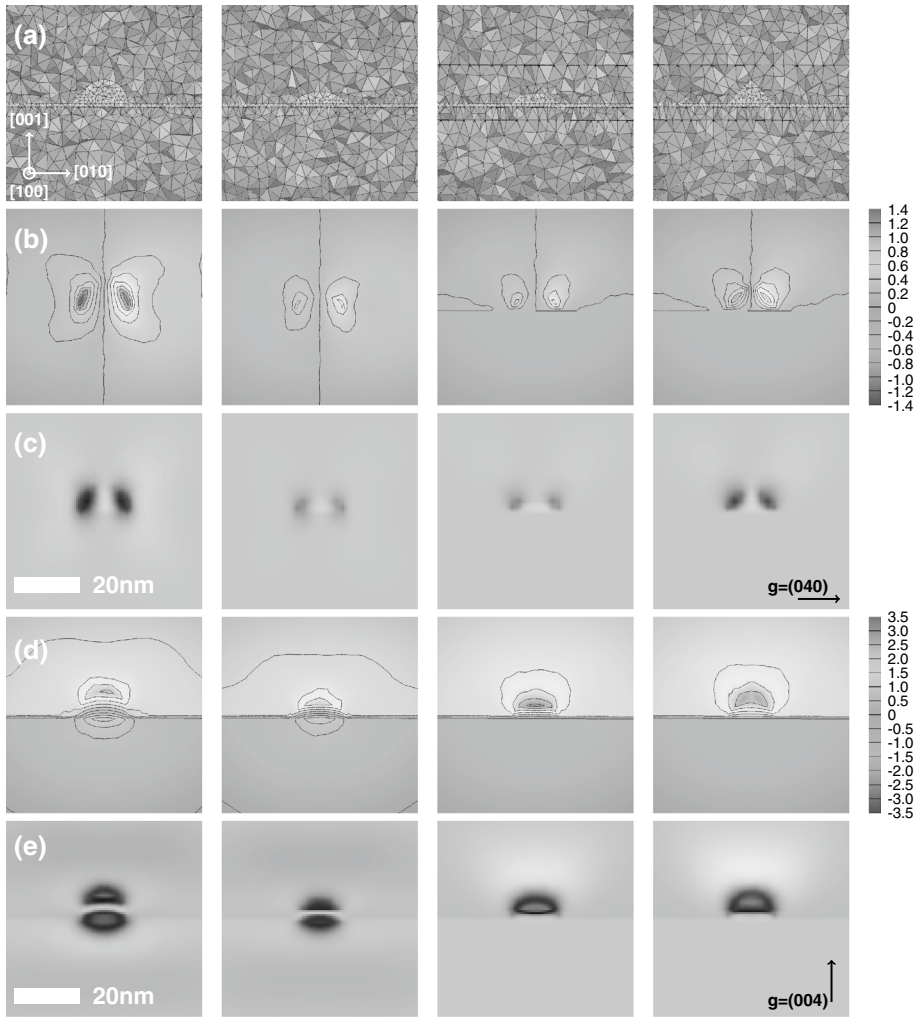


Fig. 5 InGaAs (green) quantum dots (indium content 80%) embedded in a GaAs (red) matrix with different shapes: lens-shaped QDs with circular base (two left columns) and pyramidal QDs (two right columns) with different vertical aspect ratios, respectively. FEM simulation of the elastic relaxation of the misfit induced strain: **a** geometry and FEM mesh, where we made a cut through the mesh by cell removal, so the colour changes occur due to light reflections from the remaining tetrahedra. **b** u_y component and **d** u_z component of the displacement field along a yz -cross-section through the center of the QDs in Å. The strain fields are not fully symmetric because we used an unstructured and coarse mesh. Simulated TEM images for two different excitations: **c** dark field for (040) beam for excitation under (040) two beam conditions and **e** dark field for (004) beam for excitation under (004) two beam conditions. The sample thickness is 150 nm and the acceleration voltage is 300 kV. All images show the same 60 nm × 60 nm field of view. (Color figure online)

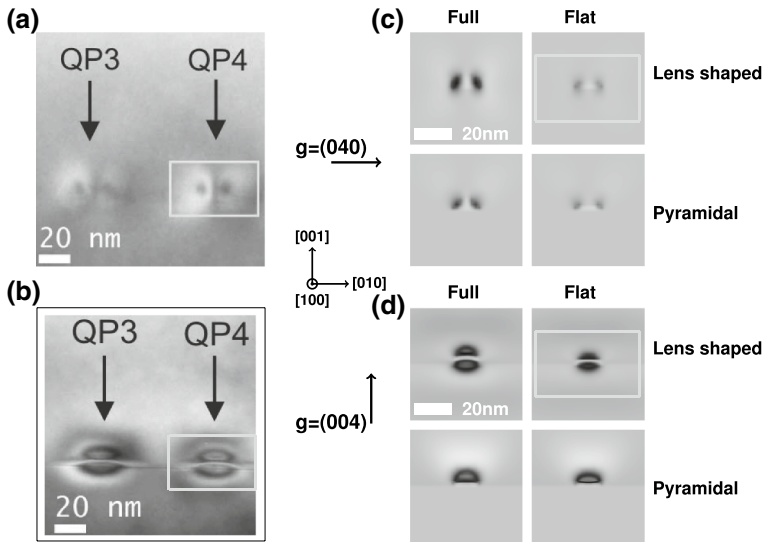


Fig. 6 Experimental images **a**, **b** from Fig. 2 compared to simulated images **c**, **d** of InGaAs quantum dots (indium content 80%) embedded in a GaAs matrix from Fig. 5. From top left to bottom right the shapes are lens-shaped, flat lens, full pyramid and truncated pyramid. Dark field images are shown for the (040) beam **a**, **c** and the (004) beam **b**, **d**. The yellow boxes indicate the same areas in both experimental and simulated TEM images. Acceleration voltage is 300 kV

4.3 Pyramidal and lens-shaped QDs

For more realistic QD TEM images we study QDs with two different shapes: lens-shaped QDs with circular base (diameter of 15 nm) and (truncated) pyramidal QDs (baselength of 15 nm) with different vertical aspect ratios, respectively, and a thin wetting layer, see Figs. 4 and 5a. We assume an indium content of 80% for all cases.

For comparison with the experimental TEM images shown in Fig. 2, we simulated TEM images for the same excitation conditions, namely (040)- and (004)-two beam conditions, see Fig. 5c, e, respectively. Consequently, the image contrast is sensitive to the y - and z -component of the displacement field, shown in Fig. 5b, d along a y z -cross section through the center of the QDs, respectively.

For both, pyramidal and lens-shaped QDs, a coffee-bean like contrast can be found for (040)-two beam conditions as it is also observed in the experimental data, see Fig. 2. However, for (004)-two-beam conditions we observe a striking difference between the images: The pyramidal QDs produce more a crescent-like contrast, whereas the contrast for the lens-shaped QDs resembles the coffee-bean contrast again. This can be explained by the different behavior of the elastic relaxation of the misfit induced strain: for lens-shaped structures the relaxation takes place in the QD as well as below and above it, while for pyramidal ones it is mainly concentrated in the QD itself and above, see Fig. 5e.

Another observation we can make from the simulated images is a line of no contrast across the center of lens-shaped QDs only. This characteristic feature is also observed experimentally, see Fig. 2. Therefore, even on the basis of the four different QD shapes we studied, one can already conclude that a lens-shaped structure matches the experimental

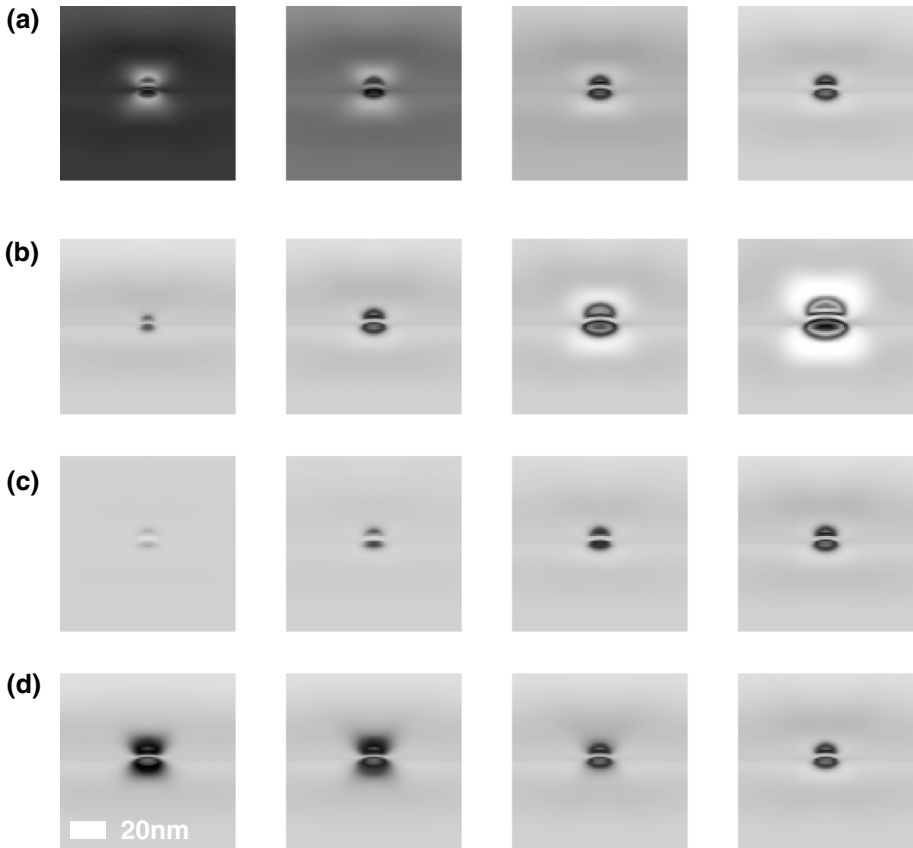


Fig. 7 InGaAs lens-shaped quantum dots embedded in a GaAs matrix. Dark field images for (040) two beam conditions: **a** thickness variation 120 nm, 130 nm, 140 nm, 150 nm, size of QD 15 nm, indium content 80%, position of QD at 75 nm, **b** size variation 10 nm, 15 nm, 20 nm, 25 nm, sample thickness 150 nm, indium content 80%, position of QD at 75 nm, **c** indium content variation 20%, 40%, 60%, 80%, sample thickness 150 nm, QD size 15 nm, position of QD at 75 nm, **d** position variation along the beam direction 45 nm, 55 nm, 65 nm, 75 nm, size of QD 15 nm, indium content 80%, sample thickness 150 nm. All images have the same gray scaling. Black corresponds to no intensity while white corresponds to the intensity of the incoming beam. Acceleration voltage is 300 kV

observations much better than pyramidal structures (truncated or not), see comparison in Fig. 6.

4.4 Database of TEM images

In order to achieve an automatic classification of QD shapes from experimental TEM images out next step is to use the tool chain to generate a database of TEM images. This database will contain series of TEM images for QDs with various shapes, in addition to pyramidal and lens-shaped, see Schliwa et al. (2007), and will depend on the size and indium concentration as well as on the excitation conditions of the electron beam, e.g. excited beam, excitation error, acceleration voltage. As an example we show a series of

specimen parameter variations for a lens-shaped InGaAs quantum dot embedded in a GaAs matrix: different values of the sample thickness in Fig. 7a, the size of the QD in Fig. 7b, the indium content in Fig. 7c and the position of the QD in the matrix relative to the top surface in Fig. 7d.

5 Conclusion

We presented a tool chain for the simulation of TEM images for QDs with realistic parameterized 3D geometries. Our computational tool chain is not restricted to QDs but can be applied also to other epitaxial heterostructures or coherent precipitates. This includes the surface relaxation of thin TEM lamellas or structures with spatially varying material composition, e.g. the QDs with varying indium content in our case.

Our study on four different QD shapes showed a strong sensitivity of image contrast to the characteristic profiles of the strain field. FEM investigations showed that the strain field in growth direction allows to distinguish between pyramidal and lens-shaped QDs. Therefore TEM images of QDs under strong beam conditions in the growth direction are suitable for the classification of QDs shapes. From comparison with experimental data we can exclude a pyramidal structure (truncated or not) for InGaAs QDs, assuming a constant homogenous indium content.

This tool chain will be used to create a database of simulated TEM images of QDs, which will serve as a training set to apply deep learning techniques. Furthermore, statistical procedures will be used to estimate continuous parameters such as height or base length of the QD for the realization of our novel concept for model-based geometry reconstruction (MBGR) of semiconductor QDs from TEM imaging. In addition, we plan to use methods like elastic shape analysis, optimal transport, diffusion maps etc, in order to define a metric on the space of TEM images and get a better understanding of its structure.

Funding Open Access funding enabled and organized by Projekt DEAL.

Open Access This article is licensed under a Creative Commons Attribution 4.0 International License, which permits use, sharing, adaptation, distribution and reproduction in any medium or format, as long as you give appropriate credit to the original author(s) and the source, provide a link to the Creative Commons licence, and indicate if changes were made. The images or other third party material in this article are included in the article's Creative Commons licence, unless indicated otherwise in a credit line to the material. If material is not included in the article's Creative Commons licence and your intended use is not permitted by statutory regulation or exceeds the permitted use, you will need to obtain permission directly from the copyright holder. To view a copy of this licence, visit <http://creativecommons.org/licenses/by/4.0/>.

References

- Benabbas, T., François, P., Androussi, Y., Lefebvre, A.: Stress relaxation in highly strained InAs/GaAs structures as studied by finite element analysis and transmission electron microscopy. *J. Appl. Phys.* **80**(5), 2763–2767 (1996). <https://doi.org/10.1063/1.363193>
- De Graef, M.: Introduction to Conventional Transmission Electron Microscopy. Cambridge University Press, Cambridge (2003). <https://doi.org/10.1017/CBO9780511615092>
- Eshelby, J.: The determination of the elastic field of an ellipsoidal inclusion, and related problems. *Proc. R. Soc. Lond. A* **241**, 376–396 (1957). <https://doi.org/10.1098/rspa.1957.0133>
- Fuhrmann, J., Streckenbach, T., et al.: pdelib: a finite volume and finite element toolbox for PDEs. <http://pdelib.org> (2019). Accessed 13 September 2019

- Hartwig, M.: TEM-Untersuchungen der Spannungsfelder von In(Ga)As-Quantenpunkten. Bachelor's thesis, TU Berlin (2011)
- Jacob, D., Androussi, Y., Benabbas, T., François, P., Lefebvre, A.: Surface relaxation of strained semiconductor heterostructures revealed by finite-element calculations and transmission electron microscopy. *Philos. Mag. A* **78**(4), 879–891 (1998). <https://doi.org/10.1080/01418619808239962>
- Koprucki, T., Malsi, A., Niermann, T., Streckenbach, T., Tabelow, K., Polzehl, J.: Towards model-based geometry reconstruction of quantum dots from TEM. In: Djurišić, A., Piprek, J. (eds.) Proceedings of the 18th International Conference on Numerical Simulation of Optoelectronic Devices (NUSOD 2018). IEEE, pp 115–116. <https://doi.org/10.1109/NUSOD.2018.8570246> (2018)
- Liao, X.Z., Zou, J., Duan, X.F., Cockayne, D.J.H., Leon, R., Lobo, C.: Transmission-electron microscopy study of the shape of buried $\text{In}_x\text{Ga}_{1-x}\text{As}$ /GaAs quantum dots. *Phys. Rev. B* **58**, R4235–R4237 (1998). <https://doi.org/10.1103/PhysRevB.58.R4235>
- Malsi, A., Koprucki, T., Niermann, T., Streckenbach, T., Tabelow, K., Polzehl, J.: Model-based geometry reconstruction of quantum dots from TEM. *Proc. Appl. Math. Mech.* **18**, e201800398 (2018). <https://doi.org/10.1002/pamm.201800398>
- Niermann, T.: pyTEM: a python-based TEM image simulation toolkit. Version 3.0.9 (2019)
- Schliwa, A., Winkelkemper, M., Bimberg, D.: Impact of size, shape, and composition on piezoelectric effects and electronic properties of In(Ga)As/GaAs quantum dots. *Phys. Rev. B* **76**, 205324 (2007). <https://doi.org/10.1103/PhysRevB.76.205324>
- Si, H.: TetGen, a Delaunay-based quality tetrahedral mesh generator. *ACM Trans. Mathe. Softw.* **41**, 1–36 (2015). <https://doi.org/10.1145/2629697>

Publisher's Note Springer Nature remains neutral with regard to jurisdictional claims in published maps and institutional affiliations.